Received: 2 July 2020 | Revised: 5 December 2020 | Accepted: 31 January 2021

DOI: 10.1002/hbm.25367

TECHNICAL REPORT

WILEY

Targeting brain regions of interest in functional near-infrared spectroscopy—Scalp-cortex correlation using subject-specific light propagation models

Lin Cai[1] | Tomonori Nitta[1] | Sho Yokota[1] | Takayuki Obata[2] | Eiji Okada[1] | Hiroshi Kawaguchi[1,2,3]

[1]Department of Electronics and Electrical Engineering, Keio University, Yokohama, Japan

[2]Department of Molecular Imaging and Theranostics, National Institute of Radiological Sciences, National Institutes for Quantum and Radiological Science and Technology, Chiba, Japan

[3]Human Informatics and Interaction Research Institute, National Institute of Advanced Industrial Science and Technology, Ibaraki, Japan

Correspondence
Hiroshi Kawaguchi, Human Information and Interaction Research Institute National Institute of Advanced Industrial Science and Technology (AIST), Central 2, 1-1-1, Umezono, Tsukuba, Japan, 305-8568
Email: hiroshi.kawaguchi@aist.go.jp

Abstract

Targeting specific brain regions of interest by the accurate positioning of optodes (emission and detection probes) on the scalp remains a challenge for functional near-infrared spectroscopy (fNIRS). Since fNIRS data does not provide any anatomical information on the brain cortex, establishing the scalp-cortex correlation (SCC) between emission-detection probe pairs on the scalp and the underlying brain regions in fNIRS measurements is extremely important. A conventional SCC is obtained by a geometrical point-to-point manner and ignores the effect of light scattering in the head tissue that occurs in actual fNIRS measurements. Here, we developed a sensitivity-based matching (SBM) method that incorporated the broad spatial sensitivity of the probe pair due to light scattering into the SCC for fNIRS. The SCC was analyzed between head surface fiducial points determined by the international 10–10 system and automated anatomical labeling brain regions for 45 subject-specific head models. The performance of the SBM method was compared with that of three conventional geometrical matching (GM) methods. We reveal that the light scattering and individual anatomical differences in the head affect the SCC, which indicates that the SBM method is compulsory to obtain the precise SCC. The SBM method enables us to evaluate the activity of cortical regions that are overlooked in the SCC obtained by conventional GM methods. Together, the SBM method could be a promising approach to guide fNIRS users in designing their probe arrangements and in explaining their measurement data.

KEYWORDS

functional near-infrared spectroscopy, inter-individual anatomical variability, light propagation, scalp-cortex correlation

This is an open access article under the terms of the Creative Commons Attribution-NonCommercial-NoDerivs License, which permits use and distribution in any medium, provided the original work is properly cited, the use is non-commercial and no modifications or adaptations are made.
© 2021 The Authors. *Human Brain Mapping* published by Wiley Periodicals LLC.

1 | INTRODUCTION

Functional near-infrared spectroscopy (fNIRS) is a noninvasive neuroimaging technique that uses near-infrared light to estimate regional neural activity indirectly by measuring local changes in the optical absorption of hemoglobin in tissue driven by blood oxygenation level changes in response to neural metabolic demand (Boas, Elwell, Ferrari, & Taga, 2014; Lloyd-Fox, Blasi, & Elwell, 2010; Quaresima, Bisconti, & Ferrari, 2012; Scholkmann et al., 2014). Multiple pairs of emission and detection probes, which illuminate and receive near-infrared light, respectively, are fixed to a subject's scalp, forming measurement channels that record hemodynamic activity occurring in the cortex below the channels. fNIRS offers a good balance between temporal and spatial resolution and is less restrictive for subjects compared to functional magnetic resonance imaging (fMRI). Therefore, it serves as a valuable neuroimaging tool for examining brain activation or functional connectivity during special tasks or specific patient populations, such as motor control (Vitorio, Stuart, Rochester, Alcock, & Pantall, 2017), person-to-person social interactions (Minagawa, Xu, & Morimoto, 2018) as well as patients with magnetic implants (Saliba, Bortfeld, Levitin, & Oghalai, 2016).

Since the function and structure of the human brain are inseparably intertwined, it is important to establish the scalp-cortex correlation (SCC) between the scalp surface positions and the underlying cortical regions for fNIRS, which only provide information that is functional, not structural. Once the SCC is available, researchers will be able to interpret fNIRS data from a spatial perspective. Furthermore, the identification of brain regions where the fNIRS signal originates from is very useful in comparing fNIRS findings with those derived from neuroscience and neuroimaging techniques, for example, fMRI of the anatomical structure.

In most fNIRS studies, fNIRS data and cortical regions are linked in a geometrical manner. A traditional approach is to attach MRI-visible markers to the probes and/or channel positions on the subject's scalp and obtain their positions through structural information from MRI. Subsequently, the most probable cortical region corresponding to each probe pair is identified by projecting each marker position to the cortical surface (Cai, Dong, & Niu, 2018; Cai, Dong, Wang, & Niu, 2019; Kovelman et al., 2009). Another widely accepted approach employs the electrode placement system that defines fiducial points on the scalp according to anatomical landmarks on the head surface, that is, the international 10–20 system. Several studies have demonstrated that there is a reasonable positional correlation between the fiducial points and the anatomical structure of the cerebral cortex (Blume, Buza, & Okazaki, 1974; Homan, Herman, & Purdy, 1987; Koessler et al., 2009; Okamoto et al., 2004). In addition, the fiducial points can be used as reference points to transfer the positions of fNIRS measurement channels to a space where a population-averaged standard brain template is in place (Tsuzuki & Dan, 2014; Tsuzuki et al., 2007). Practically, the channel position is projected to the cortical point of the standard brain template by a geometrical algorithm (Okamoto & Dan, 2005; Singh, Okamoto, Dan, Jurcak, & Dan, 2005), which is then linked to the cortical regions that are labeled on the brain atlas (Tzourio-Mazoyer et al., 2002). As a different approach to link the scalp surface positions and cortical regions, a transcranial brain atlas that presents the label of the cortical regions transferred to the scalp surface has been proposed (Xiao et al., 2018). In the process of constructing a transcranial brain atlas, the point on the scalp was geometrically projected onto the cortical surface at the subject head structure. In sum, all of the above approaches provide a correlation between the position on the scalp and the cerebral region based on a geometric point-to-point relationship. These methods assume that the absorption change, of the fNIRS measurement, in which the probe pair measures is located at the cortical projection point below the midpoint between the probe pair on the scalp.

Since near-infrared light is strongly scattered in biological tissue, a probe pair of fNIRS can indicate broad areas, not a single point in the cerebral cortex. However, some studies have begun to analyze the SCC by estimating the penetration of near-infrared light into the subject's head (Machado et al., 2018; Morais, Balardin, & Sato, 2018). Notably, the propagation of near-infrared light in head tissues has also been investigated in detail using computer simulation. To characterize the sensitivity of the fNIRS signal to the absorption change in the volume of sampled tissue, a spatial sensitivity profile (SSP) on the surface of the gray matter for one probe pair is usually obtained by the Monte Carlo simulation or the diffusion theory (Quaresima & Ferrari, 2019). The SSP on the surface of the gray matter shows the greatest value at just below the midpoint of the pair of emission and detection probes, and the probe pair detects the absorption change in a broad region of the gray matter (Kawaguchi, Hayashi, Kato, & Okada, 2004; Sakakibara, Kurihara, & Okada, 2016). Such light propagation within a tissue is influenced by factors such as optical properties of tissue and the anatomical structure of the brain and extracerebral tissues (M. Firbank, Okada, & Delpy, 1998; Koyama, Iwasaki, Ogoshi, & Okada, 2005; Okada et al., 1997; Strangman, Franceschini, & Boas, 2003). The structural variations in terms of cortical folding, head size and skull thickness also influence fNIRS sensitivity to brain activity. Several studies have shown that the anatomical structure affects the sensitivity of the fNIRS signal by using realistic 3D head models (Custo, Wells, Barnett, Hillman, & Boas, 2006; Fukui, Ajichi, & Okada, 2003; Hoshi, Shimada, Sato, & Iguchi, 2005; Strangman et al., 2003). In particular, by constructing subject-specific head models, Nakamura et al. found that variability of the partial optical pathlength in the brain was very high between subjects and between fiducial points, and that partial optical pathlength was strongly associated with the depth of the brain surface (Nakamura et al., 2016). Moreover, the partial optical pathlength of the fNIRS probe pair depends not only on the individual's head structure, but also on the local head structure to which the probe is attached, even for the same individual subject. Therefore, the SCC should be elucidated based on light propagation with consideration given to individual differences in head structure. In addition, the orientation in which the probe pair is attached around the fiducial point, for example, the vertical or circumferential direction with the fiducial point as the center, can influence the analysis of brain regions where the probe pair is sensitive.

In the current study, we analyzed the impact of light scattering in the adult human head on the correlation between scalp fiducial points and cortical regions. Forty-five adult subject-specific head models for light propagation analysis were constructed from structural MRI images. The whole-brain volumes of the models were parcellated into 116 cortical regions according to the brain atlas. The sensitivity to cortical regions was obtained for each fNIRS probe pair placed at the fiducial point on the scalp by solving the diffusion equation. We also analyzed the effect of inter-subject anatomical variability and probe-pair orientation around the fiducial points on the sensitivity-based correlation. In addition, the sensitivity-based correlation at each fiducial point was compared with the SCC obtained with conventional geometrical methods.

2 | MATERIALS AND METHODS

2.1 | Light propagation analysis of the subject-specific models

2.1.1 | MRI acquisition

Structural MRI scans were performed to analyze the SCC based on the individual head structure of the subjects and the optical heterogeneity of the tissue. Forty-five healthy mongoloid adults (23 males and 22 females, aged 21–58 years, mean and standard deviation of 37.7 ± 11.5) participated in this study after providing written informed consent. All MRI data in this study were from our previous study (Kurihara, Kawaguchi, Obata, Ito, & Okada, 2015). The study protocol was approved by the Ethics and Radiation Safety Committees of the National Institute of Radiological Sciences, Chiba, Japan. This study adheres to the declaration of Helsinki. All participants in this study gave their written informed consent before MRI acquisition. (Clinical trial registration: UMIN Clinical Trials Registry [ID: UMIN000004588]).

All the MR experiments were performed using a 3.0-T clinical MR system (SignaHDx 3.0; GE Healthcare, Milwaukee, WI) to acquire T1-weighted (TIW), fat-saturated proton density weighted (FS-PDW) and fast imaging employing steady-state acquisition (FIESTA) images. The detailed scan parameters of the three contrast variant images were as follows: (a) T1W, 3-dimensional spoiled gradient echo (3D-SPGR) with inversion pulse and array spatial sensitivity encoding technique (ASSET), repetition time (TR)/echo time (TE)/inversion time (TI) = 6.8/1.9/450 ms, flip angle (FA) = 12°, matrix = 256 × 256, number of excitation (NEX) = 1; (b) FS-PDW, 3D-SPGR with ASSET and tailored radiofrequency pulse for FS, TR/TE = 13.8/1.9 ms, FA = 6°, matrix = 256 × 256, NEX = 1; (c) FIESTA, TR/TE = 13.8/1.9, FA = 45°, matrix = 256 × 256, NEX = 1. ASSET factor of 2 was applied to all sequences using ASSET. The field of view and slice thickness of all the images was 26.0 cm and 1.0 mm, respectively. All the image data were anonymized prior to the segmentation process.

2.1.2 | Construction of subject-specific head models

The procedure for constructing the head model was based on our previous work (Kurihara et al., 2015). T1W images have a good contrast, which enables segmentation of the intracranial regions, that is, cerebrospinal fluid (CSF), gray matter, and white matter. However, it has no contrast between the skull and CSF. FS-PDW and FIESTA images provide good contrast to segment superficial layers such as the scalp, skull, and CSF. The FS-PDW image has a low signal intensity at the skull and a high signal intensity from the scalp and CSF. It provides a good contrast between the scalp and skull, and between the skull and CSF (Keller, Hunter Jr, & Schmalbrock, 1987). Thus, the air/scalp, scalp/skull, and skull/CSF boundaries were extracted from the FS-PDW images. Since the CSF has a higher signal intensity than other tissue types in the FIESTA image, the CSF/brain boundaries could be easily distinguished using the image contrast (Schmitz, Hagen, & Reith, 2003). The brain region was extracted from the FIESTA image and then segmented into the gray matter and white matter regions using the T1W image by the FMRIB's Automated Segmentation Tool (FAST; Zhang, Brady, & Smith, 2001). The extra-cerebral regions were segmented by binarization and morphological operations (For more details, see Kurihara et al., 2015). The anatomical structure of the representative 5-layered subject-specific model is shown in Figure 1.

2.1.3 | Light propagation analysis

The volumetric tetrahedral mesh for each segmented 3D head model was generated by the iso2mesh toolbox (Fang & Boas, 2009) for light propagation analysis by the diffusion equation using the finite element method. The light propagation in the head models was calculated by Nirfast, a finite element-based package that uses a diffusion approximation for modeling near-infrared light transport in tissue (Dehghani et al., 2009; Jermyn et al., 2013). Optical properties in every tissue layer of head models were specified from the reported data for each type of tissue, that is, scalp (Torricelli, Pifferi, Taroni, Giambattistelli, & Cubeddu, 2001); skull (Bevilacqua et al., 1999; Firbank, 1994); CSF (Hale & Querry, 1973; Okada & Delpy, 2003a); gray matter; and white matter (Bevilacqua et al., 1999; Gebhart, Lin, & Mahadevan-Jansen, 2006) at an 800-nm wavelength as shown in Table 1.

2.2 | Definition of scalp positions and cortical regions

2.2.1 | Scalp fiducial points and probe-pair orientation

Numerous researchers in the fNIRS community have adopted the 10–10 or 10–20 system to position their probe pairs to detect targeted brain regions (Anderson, Wiggins, Kitterick, & Hartley, 2017;

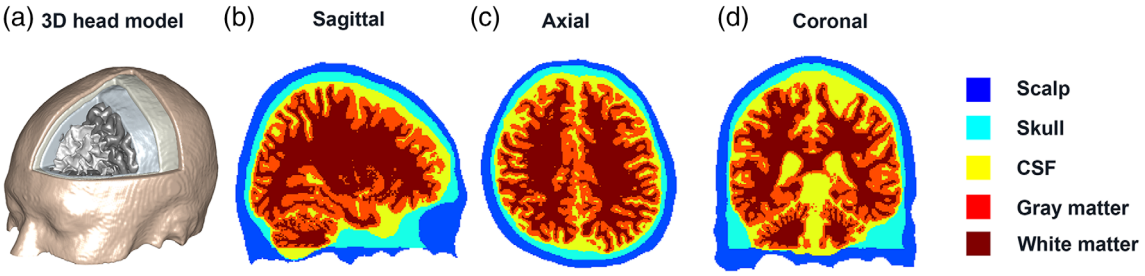

FIGURE 1 The five-layered subject-specific realistic head model for the light propagation calculation. MR images were segmented into the scalp, skull, cerebrospinal fluid, gray matter, and white matter to construct the model. (a) Three-dimensional segmented geometry of a realistic head model for one representative subject. (b–d) The segmented images for different slice views from the same subject

TABLE 1 The optical properties of light propagation in various tissues using head models

	Absorption coefficient (mm^{-1})	Transport scattering coefficient (mm^{-1})
Scalp	.016	1.35
Skull	.01	.98
CSF	.004	.30
Gray matter	.019	.86
White matter	.011	4.16

Jiang et al., 2015; Minagawa-Kawai, Mori, Naoi, & Kojima, 2007; Moriguchi & Hiraki, 2009). As such, we analyzed the SCC at the fiducial points of the 10–10 system. Specifically, we firstly identified the coordinates of anatomical landmarks corresponding to the inion, nasion, and left and right periauricular points manually in each subject-specific head model. Then we set all of 61 fiducial points on the scalp of the head model according to the unambiguously illustrated 10–10 system developed by Dan's group (Jurcak, Tsuzuki, & Dan, 2007) as shown in Figure 2a. To examine whether the probe-pair orientation influenced the SCC, two probe pairs were placed in a circumferential and vertical orientation at each fiducial point. The distance between the emission and detection probes was set as 30 mm which has been identified as the optimal probe spacing for adult fNIRS studies (Strangman, Li, & Zhang, 2013), and the midpoint of the probes was set on the fiducial points. The probe positions as rendered in a head model with different views are shown in Figure 2b–f.

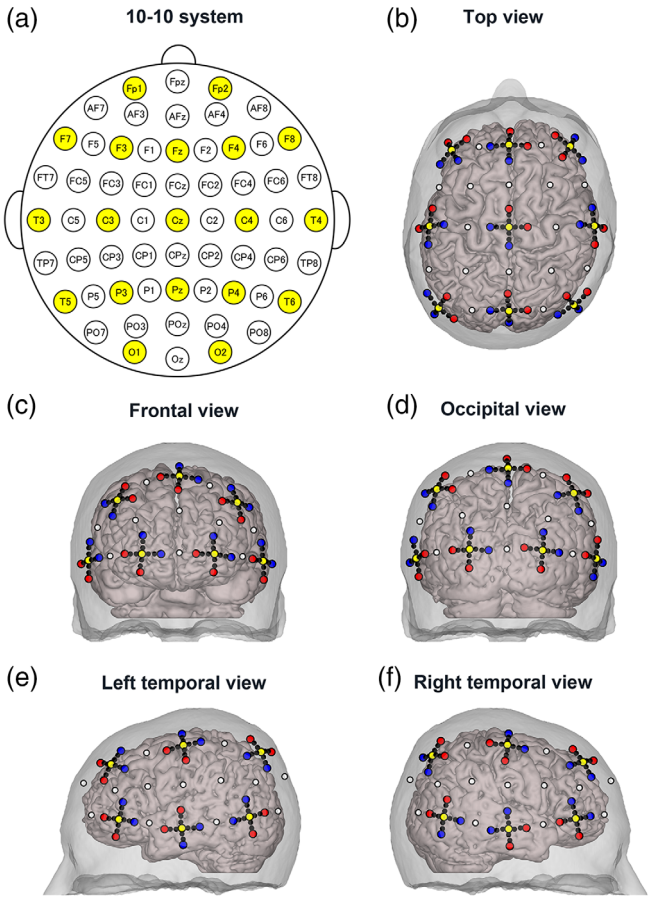

FIGURE 2 The arrangement of probe pairs according to the 10–10 system. (a) 61 fiducial points of the 10–10 system, in which 10–20 positions were filled with yellow color. (b–f) the arrangement of two orientational probe pairs at 10–20 fiducial points (yellow dots) superposed on the surface of one subject's scalp for different views. The emission and detection probes are indicated by red and blue circles, respectively. Black dotted lines are used for displaying circumferential and vertical probe pairs. Note that probe pairs were also attached on the 10–10 fiducial points (white dots), but were not shown to avoid complications

2.2.2 | Individual brain parcellation

To compute the SCC at the individual level, we needed to parcellate the brain into different multiple nonoverlapping brain regions for every subject. Because it is time-consuming to parcellate each individual brain by manual delineation, we developed a semi-automatic pipeline to parcellate the brain of 45 subjects. Herein, the automated anatomical labeling (AAL) atlas that parcellates a human brain according to the macro-anatomical structure (Rolls, Joliot, & Tzourio-Mazoyer, 2015; Tzourio-Mazoyer et al., 2002) was transferred onto the brain of each individual subject (Figure 3). Given that the AAL atlas was generated using a single subject brain in MNI space, Colin27, we chose the ICBM-152 brain template defined in the MNI

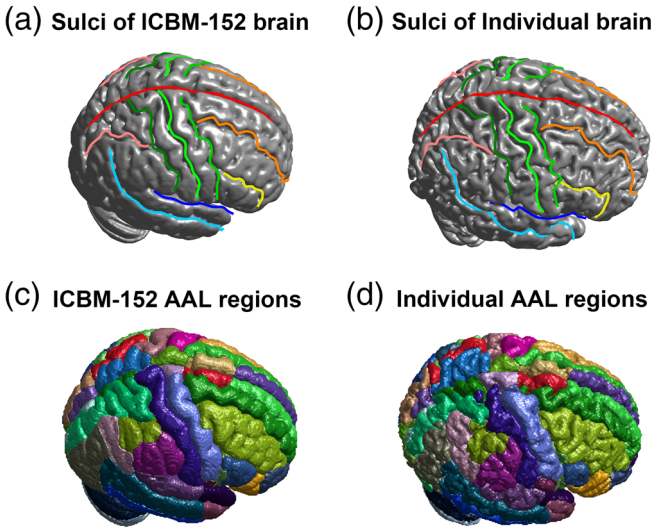

FIGURE 3 Parcellation of individual brains according to the automated anatomical labeling (AAL) atlas. The 17 major sulci were identified on the structures of the ICBM-152 brain template (a) and the brains of the 45 individual subjects. The brain structure and sulci of a representative subject are shown in (b). The sulcal positions were used to accurately transform the ICBM-152 brain template into each individual brain. The AAL regions on the ICBM-152 brain template (c) were transferred to the individual brain by applying the transformation functions based on the brain structure and sulcal positions. The AAL regions of a representative subject are shown in (d)

coordinates as a reference brain to parcellate the individual brain. The ICBM-152 has been demonstrated to be the best template for the description of scalp positions and their correlation to MNI coordinates of the underlying cerebral structures by combining both high spatial resolution and signal-to-noise while avoiding the "single brain" criticism subject to the vagaries of any single brain (Cutini, Scatturin, & Zorzi, 2011; Huang, Parra, & Haufe, 2016). Since the AAL atlas is based on gyri and sulci, we first extracted the 17 major sulci as landmarks from both the ICBM-152 brain template (Figure 3a) and the individual brains (Figure 3b). Here, the 17 sulci were longitudinal fissure, bilateral central sulcus, bilateral precentral sulcus, bilateral postcentral sulcus, bilateral superior frontal sulcus, bilateral inferior frontal sulcus, bilateral sylvian fissure, bilateral superior temporal sulcus, and bilateral intraparietal sulcus. Next, we transformed the brain template with 17 sulci to align with the individual brain with 17 sulci by SPM DARTEL (Ashburner, 2007). However, the sulci of the transformed brain template misaligned slightly with those of the individual brain. Hence, we applied a radial basis functional transform (RBFT) algorithm (Pighin, Hecker, Lischinski, Szeliski, & Salesin, 2006), which uses sulcal positions as anchor points to further reshape the transformed brain template to align with the individual brain, so that the AAL brain regions on the brain template were transferred onto the structure of the individual brain. The combination of DARTEL with a transformation based on the shape of the sulci improved the consistency and accuracy of the alignment performance (Auzias et al., 2011). Finally, 116 brain regions on the AAL atlas (Table S1) were transferred from the brain template (Figure 3c) to the individual brain (Figure 3d) using transformation functions obtained by SPM DARTEL and RBFT. The above pipeline was repeated for the brain structures of the 45 subjects. That is, the brains of 45 subjects were parcellated according to the macroanatomical definition of the AAL atlas. Using the 45 subject-specific head models, we could analyze the effect of inter-subject anatomical variability on the correlation between scalp surface fiducial points and brain regions. Each node of the tetrahedral mesh was labeled as a specific AAL region for each subject.

2.3 | Methodologies to analyze the SCC

The correlation between scalp fiducial points and brain regions was analyzed by a method based on light propagation in an adult head and three geometrical methods (Figure 4). The SCC was analyzed in two steps for either matching method. Sensitivity-based matching (SBM) provides the SCC based on the SSP of the probe-pair at each scalp fiducial point. In geometrical matching (GM), SCC was obtained geometrically by using an approximated perpendicular line from the scalp surface at each fiducial point. There are three types of GM methods according to the space in which each step is executed. Details of each matching method are described below.

2.3.1 | Sensitivity-based matching

SBM was defined as a methodology to analyze the SCC based on a light propagation analysis of the adult head (Figure 4a). At first, the photon measurement density function (PMDF) was calculated at each node of the mesh model based on the results obtained from a light propagation analysis (Arridge, 1995). Under the conditions in the light propagation analysis of this study, the PMDF had the same spatial distribution as the SSP (Oki, Kawaguchi, & Okada, 2009). Since the SSP can be considered the partial optical pathlength in a small volume, the sum of the SSP in a brain region is equivalent to the partial optical pathlength of the same region. In other words, the sum of PMDF in a brain region is linearly related to the partial optical pathlength within the same region. We then calculated the proportion of partial optical pathlengths for a given brain region M in all 116 brain regions (L_M) using the following equation as a metric of the sensitivity-based correlation,

$$L_M = \frac{l_M}{\sum_{j=1}^{N} l_j},$$

where l_M and l_j is the sum of PMDF of all nodes within the brain regions M and j, respectively. N is the number of brain regions within the whole brain tissue. As PMDF is a probability density function (Arridge & Schweiger, 1995), the L_M is regarded as the probability that the fNIRS signal is affected by the brain activation of the region M. The L_M was calculated for circumferential and vertical probe-pair orientations at every fiducial point for all 45 subjects. Note that the

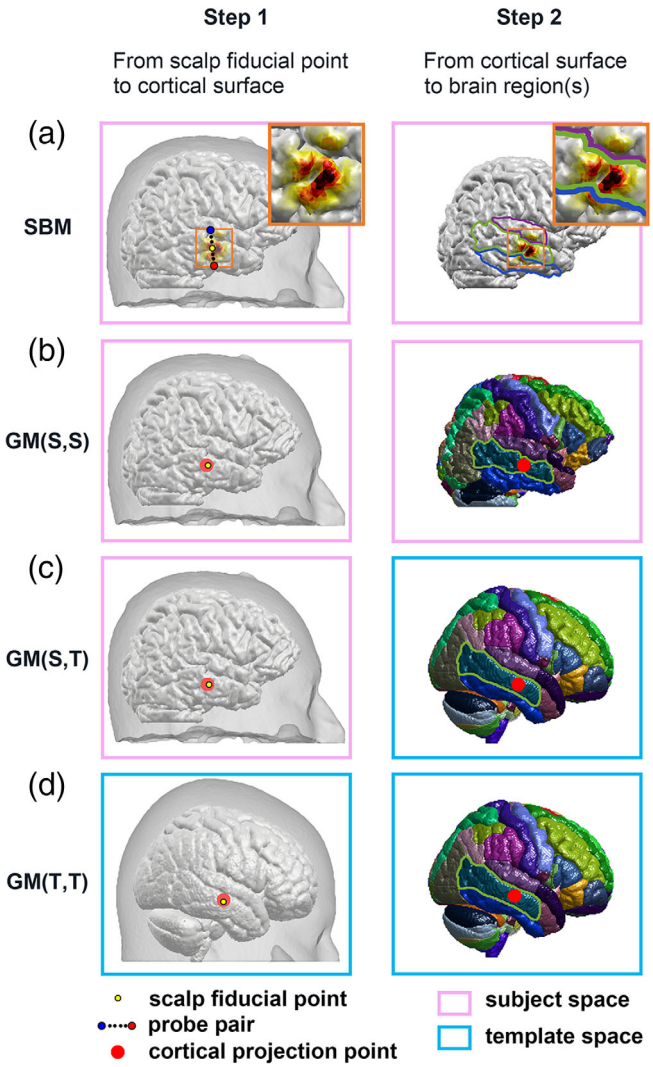

FIGURE 4 Methods to analyze the scalp-cortex correlation (SCC). (a) sensitivity-based matching (SBM), (b) geometrical matching (GM) (S,S), (c) GM (S,T), and (d) GM (T,T). In (a), the spatial sensitivity profile of the probe pair was represented by magnification of the gray matter surface. The colors in descending order of sensitivity are black, red and yellow. The first and second character in the brackets of GM corresponds to the space in which the first and second steps of the SCC were executed, that is, S and T denote the subject space and template space, respectively

45 subject-specific individual head models with unique individual brain parcellation were used to obtain the L_M.

2.3.2 | Geometrical matchings

GM, which assumes the fNIRS signal is mainly contributed from the midpoint between the emission and detection probes, has been widely adopted to analyze the SCC in fNIRS studies. GM consists of two steps to analyze the SCC (Figure 4b–d). Initially, the scalp position is projected onto the cortical surface location (Figure 4b–d, left panel). Next, the brain region to which the cortical location belongs is determined according to the brain atlas (Figure 4b–d, right panel). Based on whether these two steps were executed in the subject-specific spaces or the template space, we defined three GMs: GM (S,S), GM (S,T) and GM (T,T), in which S and T indicate subject-specific spaces and the template spaces, respectively. GM (S,S) corresponds to a traditional approach in which markers attached to probes are imaged with an MRI scan and then each marker position is projected onto the cortical surface along with the individual brain structure. GM (S,T) is included in the procedure to construct the transcranial brain atlas (Xiao et al., 2018). According to the definition of GM (T,T), it is assumed that GM (T,T) is a probabilistic registration (Singh et al., 2005; Tsuzuki & Dan, 2014).

GM (S,S) and GM (S,T) projected the 10–10 fiducial points on the scalp surface of each individual subject to the cortical surface points in the individual space (Figure 4b,c, left panels) by the balloon-inflation algorithm (Okamoto & Dan, 2005). For GM (S,S), the AAL brain region closest to the projected cortical surface point in the individual space was determined as the corresponding brain region for each fiducial point (Figure 4b, right panel). For GM (S,T), however, we used a spatial normalization process to transfer the coordinates of cortical surface points to a MNI space by SPM DARTEL (Figure 4c, right panel), which was similar to the approach taken in a recent study (Xiao et al., 2018). Subsequently, the AAL brain region closest to the transferred point was searched in the ICBM-152 brain template. Finally, the closest region in the template was assigned as the corresponded brain region for each fiducial point. GM (S,S) and GM (S,T) make each fiducial point of individual subject correspond to a single brain region. In other words, the probability that the fNIRS signal is affected by brain activation in that single region is 1. We employed these probabilities as a metric of the SCC for GM (S,S) and GM (S,T). We repeated the above steps for all 45 subjects to obtain the probability of the corresponding brain region at every fiducial point for GM (S,S) and GM (S,T), independently.

The SCC of GM (T,T) was analyzed using an NFRI toolbox (Okamoto et al., 2004; Okamoto & Dan, 2005; Singh et al., 2005). At the individual level, the coordinates of all 10–10 fiducial points were firstly affine-transformed to the corresponding coordinates on the scalp in the MNI space using the MRI database, which consists of 17 reference brains. Next, those transferred points were projected onto the cortical surfaces of those reference brains (Figure 4d, left panel) by the balloon-inflation method (Okamoto & Dan, 2005). The spatial distribution of the projected cortical points was then quantified by the average and standard deviation from the 17 reference brains. Finally, the proportion of each brain region covered by the spatial distribution as a metric of the SCC for GM(T,T) was provided using an AAL atlas (Figure 4d, right panel).

Three GMs can be clearly ordered according to methodological differences from SBM (Figure 4). As the PMDF of each brain region is calculated using SBM in the subject-specific model, the methodological dissociation for SBM and GM (S, S) was the difference in consideration of the light scattering (Figure 4a,b). In addition the light scattering was not considered, GM (S,T) was different from SBM at the point that the brain labeling of the cortical location was

determined using the template (Figure 4a,c). In addition to the differences between SBM and GM (S,T), GM (T,T) differed from SBM at the point that the scalp position was projected onto the cortical surface in the template brain (Figure 4a,d). Thus, the methodological dissociation between SBM and GMs increased in the order of GM (S,S), GM (S,T), and GM (T,T).

2.4 | Comparisons of the SCC between SBM and GMs

2.4.1 | Comparison at the individual level

The measures of the SCC obtained by SBM and GMs can be regarded as a probability showing which brain region the fNIRS signal derives from. That is, they can be compared directly at the individual level. In addition, it would be interesting for fNIRS users to know which brain region is the most likely source of the signal. The most likely corresponding brain region (MLCBR) was defined for each matching method; that is the brain region with the largest L_M for SBM, the brain region obtained by the methods themselves for GM (S,S) and GM (S,T), and the brain region with the highest volumetric occupancy in the sphere centered on the centroid of the projected cortical points for GM (T,T).

2.4.2 | Comparison at the group level

The group-level SCC indices were calculated at each fiducial point for the group-level comparisons of matching methods. One of the group-level SCC indices used was the group-wise probability of corresponding brain region for each matching method, that is, the average of the L_M across all subjects for SBM, the number of subjects corresponding to a specific brain region divided by the total number of subjects for GM (S,S) and GM (S,T) and the score calculated by the group analysis of NFRI toolbox for GM (T,T). The group-wise probability of GM (T,T) was obtained from a multi-subject spatial distribution of cortical points corresponding to a given fiducial point by using spatial distribution results from all individual subjects. To statistically compare the group-wise probability between SBM and each GM, that is, SBM versus GM (S,S), SBM versus GM (S,T), and SBM versus GM (T,T), we used the chi-square test of independence, which is often used to determine if there is a significant relationship between two nominal variables. In this study, the null hypothesis was that there would be no relationship between the group-wise probability between SBM and those from GMs. On the contrary, the alternative hypothesis was that there would be an association between the group-wise probabilities from different methods. The rejection of the null hypothesis meant that the proportion distribution of a series of corresponding AAL brain regions was distinct between SBM and GM at a fiducial point. Dunnett's test was adopted to hold the familywise error rate at or below alpha significant level (i.e., .05, .01, .001) when performing multiple comparisons of SBM with each GM (Dunnett, 1955). Moreover, in order to examine the effect of the probe-pair orientation on the sensitivity-based correlation, we also performed the chi-square test of independence between the group-wise probabilities from circumferential and vertical orientations for SBM.

The group-wise MLCBR was also obtained as another group-level SCC index. The group-wise MLCBR was the AAL region corresponding to the maximum group-wise probability of each matching method. In addition, we defined the concordance rate Q representing the extent of consistency of the MLCBR between SBM and each GM;

$$Q = \frac{n}{N} \times 100,$$

where n was the number of subjects that had the same MLCBR between SBM and GMs and N was the total number of subjects.

3 | RESULTS

3.1 | Impact of the light scattering and probe-pair orientation on the SCC

For an arbitrarily chosen subject, the PMDF of two probe-pair orientations, which were set at the fiducial point T4, are shown in Figure 5a. T4 corresponded to three brain regions (MTG_R: 0.689; ITG_R: 0.228; STG_R: 0.082) for circumferential orientation (Figure 5A, upper panel). Similarly, the same brain regions with slightly different L_M (MTG_R: 0.692; ITG_R: 0.242; STG_R: 0.065) were corresponded when examining vertical orientation (Figure 5a, lower panel). Importantly, even for the same fiducial point T4, the brain regions with sensitivity varied across subjects (Figure 5b). Similar spatial patterns of PMDF for one specific subject (Figure 5a) and L_M distribution for all subjects (each column of matrix indicating the L_M distribution of one subject, Figure 5b) showed that the sensitivity-based correlation seemed independent of the probe-pair orientations. Moreover, results from other fiducial points, F8 and O1, also showed that two L_M matrices of two different orientations were highly similar by visual examination (Figure 5c,d). Further chi-square test of independence at the group level showed that the probe-pair orientation had no significant differences on the L_M distribution at all fiducial points, that is, all p-values were greater than .05. In addition, the inter-class correlation coefficient (ICC(2,1)) between the L_M of the MLCBR for circumferential and vertical orientations at all fiducial points was .964 (Figure 5e). The L_M of the MLCBR at most fiducial points was approximately 50% or less, in particular, those fiducial points along the Nz-Cz-Iz midline of the brain. In contrast, the L_M of the MLCBR was relatively high (>0.790) at fiducial points PO7, F3, F4, and FC3.

3.2 | A systematic comparison of sensitivity-based correlation and geometrical correlations

3.2.1 | Comparison at the individual level

Due to no significant differences between two probe-pair orientations (Section 3.1), we only chose sensitivity-based correlation from the

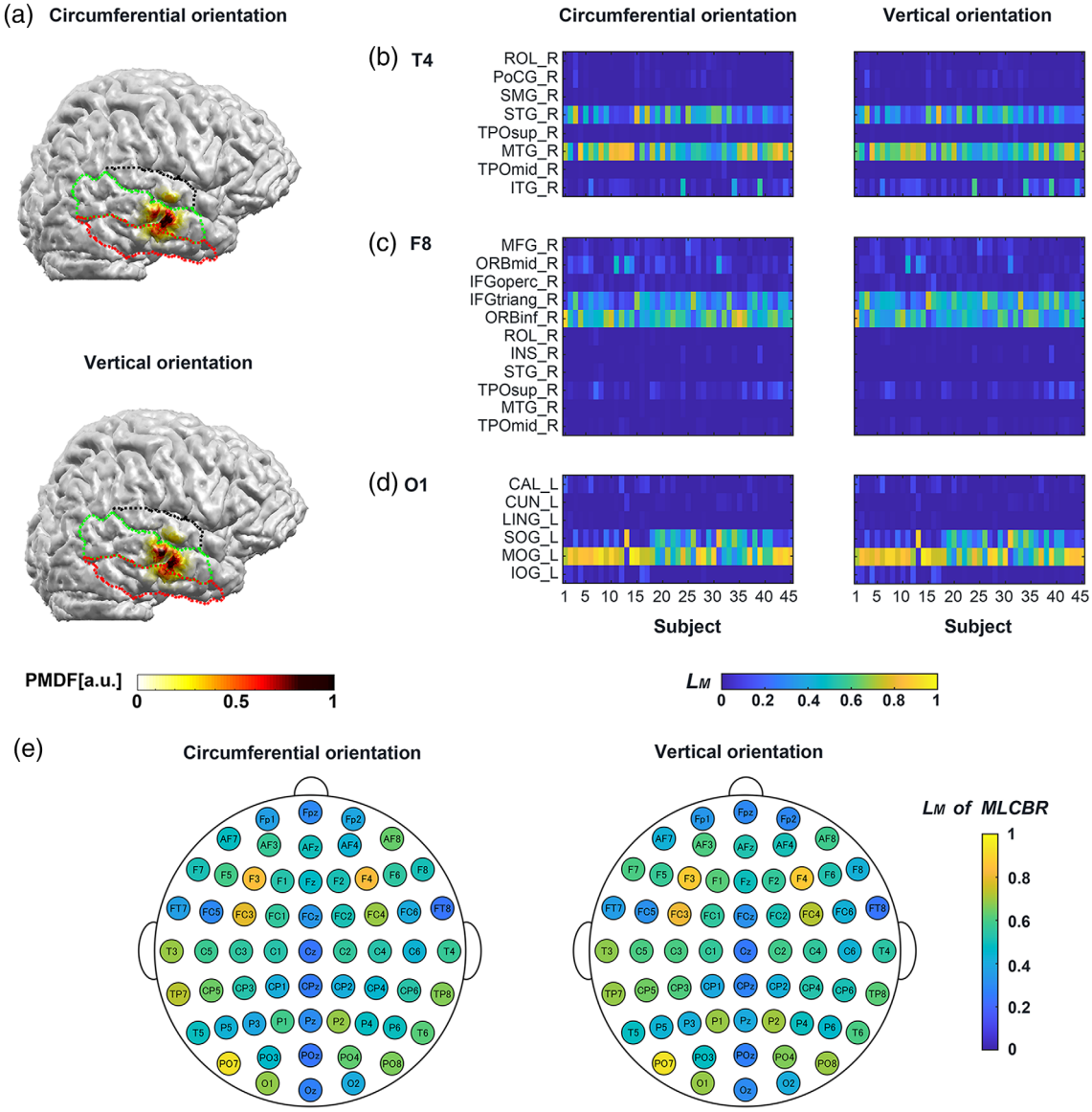

FIGURE 5 The effect of light scattering and probe-pair orientation on the scalp-cortex correlation (SCC) obtained using sensitivity-based matching (SBM). (a) The photon measurement density function (PMDF) of two probe pairs attached according to circumferential and vertical orientations at the fiducial point T4 are shown for arbitrarily chosen subject 06. Dashed lines in different colors indicate the boundaries of brain regions (i.e., red: ITG_R; green: MTG_R; black: STG_R). Two-column panels of L_M matrices at three fiducial points (b) T4, (c) F8, and (d) O1 display the L_M distribution for circumferential and vertical probe-pair orientations, respectively. The digits and characters in each L_M matrix represent the identification number of subjects and brain regions, respectively. (e) L_M of the MLCBR at all fiducial points for circumferential and vertical orientations

circumferential orientation to make the comparisons with geometrical correlations in the following sections.

To illustrate the distinction between SBM and GMs at the individual level, we selected the SCC results from three representative participants for a given fiducial point T3. The PMDF for the three subjects are shown in Figure 6a–c, respectively. Based on the L_M in brain regions, results from SBM showed that T3 corresponded to two brain regions (MTG_L: 0.757 and STG_L: 0.237) for subject 01. However, T3 had four corresponding brain regions for subject 16 (MTG_L: 0.517; STG_L: 0.445; PoCG_L: 0.019 and ROL_L: 0.012) and three corresponding brain regions for subject 44 (STG_L: 0.558; MTG_L: 0.353 and PoCG_L: 0.071), respectively. Of note, despite the probe pair being placed at the same fiducial point T3, the MLCBR was not the same among the three subjects, that is, MTG_L for subject 01 and subject 16, but STG_L for subject 44. Moreover, T3 of subject 16 had almost equivalent sensitivity for the two brain regions, but one brain region dominated for the other two subjects. The cortical positions indicating the corresponding brain region of GM (S,S) were located in the regions with the high PMDF (the green dots in Figure 6 A, B and C). Moreover, the corresponding brain region from GM (S,S) was the same as that with the largest L_M obtained by SBM for subject 01 and subject 44, except for subject 16. Nevertheless, once the spatial

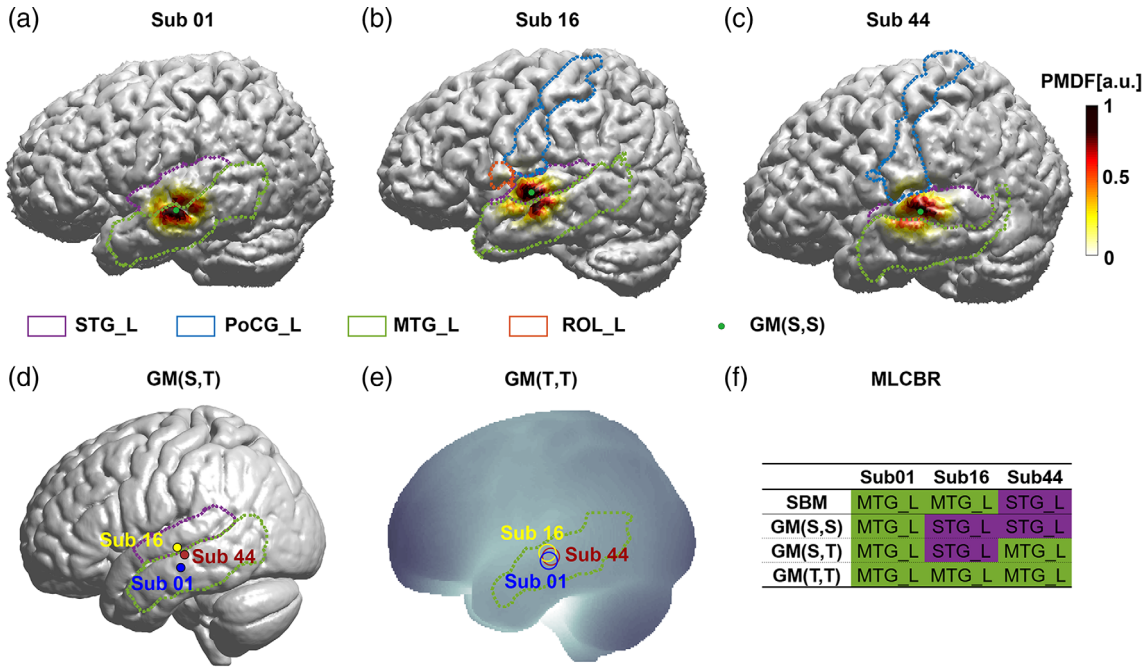

	Sub01	Sub16	Sub44
SBM	MTG_L	MTG_L	STG_L
GM(S,S)	MTG_L	STG_L	STG_L
GM(S,T)	MTG_L	STG_L	MTG_L
GM(T,T)	MTG_L	MTG_L	MTG_L

FIGURE 6 The scalp-cortex correlation (SCC) for a given fiducial point T3 of three representative subjects. Dashed lines in different colors indicate the boundaries of AAL brain regions. The photon measurement density function (PMDF) superimposed on three subject-brain structures are shown in (a–c) when the probe pair was attached in a circumferential orientation. The PMDF was normalized by the maximum value for each subject. The position identified by geometrical matching (GM) (S,S) is indicated by a green dot in (a–c). (d) Cortical surface points identified by GM (S,T) are shown as small dots on the ICBM-152 brain with different colors for three subjects. (e) The corresponding brain region obtained by GM (T,T) was displayed on the averaged reference brain. (f) The MLCBR of T3 was shown as a table for each matching method and subject. Centers and radii of circles indicate the mean values and one standard deviation of the most likely coordinates

normalization was incorporated into the calculation of the SCC, as in GM (S,T), only the corresponding brain region of subject 01 was the same as that of the largest L_M (Figure 6d). As shown in results from GM (T,T) (Figure 6e), T3 corresponded to the same brain region MTG_L for the three subjects, in which corresponding brain regions of subject 01 and subject 16 were congruent with those with the largest L_M. Figure 6f summarized the results of MLCBR for each matching method and subject.

To investigate the SCC systematically at fiducial points of each matching method across all 45 subjects, we selected three fiducial points (T3, Fpz, and Cz) that have widely been used as reference points to attach probes in cognitive neuroscience studies using fNIRS. For the fiducial point T3, the number of the corresponding brain regions was different between subjects when SBM was used (max: 7 regions; min: 2 regions, see Figure 7a upper panel). GM (S,S) and GM (S,T) provided the single corresponding region since these methods were based on the point-to-point correlation at the individual level. GM (T,T) showed that T3 focused on one or two specific brain regions, for example, MTG_L, 0.847; ITG_L, 0.153 for subject 13; MTG_L, 1.000 for subject 18. The SCC at Fpz and Cz displayed a large discrepancy compared to T3. Specifically, the number of brain regions that Fpz and Cz corresponded to was much larger than that of T3 using SBM. In addition, the L_M of Fpz and Cz was not exclusively high in one region, but it was broadly distributed across several regions (Figure 7b,c, upper panel). The corresponding brain region of GM (S,S) and GM (S,T) varied across subjects and the inter-subject variability differed at fiducial points (Figure 7b,c, upper panel). GM (T,T) showed that corresponding brain regions had more relatively limited and focused distribution across subjects (Figure 7b,c, upper panel).

The MLCBR at T3 between SBM and each GM was distinct only in a few subjects. (Figure 7a, lower panel). In contrast, the MLCBR at Fpz or Cz was inconsistent between SBM and all GMs for most subjects (Figure 7 B and C, lower panel). Furthermore, the inconsistency of the MLCBR at each fiducial point increased with larger methodological dissociation between SBM and GMs. For instance, the number of subjects for whom the MLCBR was consistent between SBM and GMs (the number of yellow blocks in the lower panel of Figure 7) decreased at T3, that is, 44, 41, and 39 for SBM versus GM (S,S), SBM versus GM (S,T), and SBM versus GM(T,T), respectively. On the other hand, the consistency of the MLCBR between SBM and each GM was different at chosen fiducial points, as indicated by the decrease in yellow blocks from T3, Fpz to Cz (Figure 7a–c, lower panel).

3.2.2 | Comparison at the group level

To examine the differences among SBM and GMs at the group level, we calculated group-level SCC indices across 45 subjects at three fiducial points T3, Fpz, and Cz (Table 2). We found T3 had three

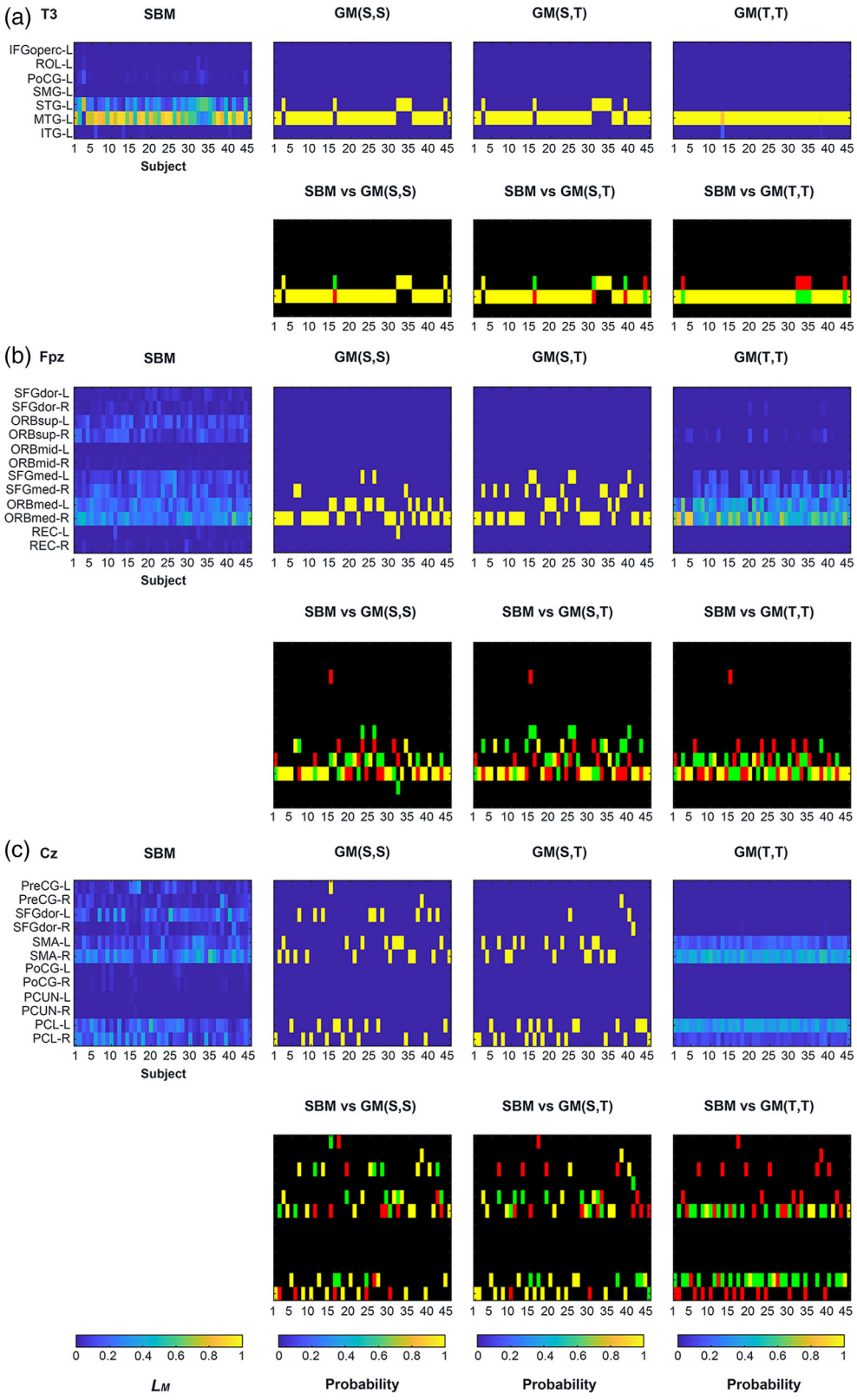

FIGURE 7 The matrices indicating the scalp-cortex correlation (SCC) obtained by sensitivity-based matching (SBM) and three geometrical matchings (GMs) at three representative fiducial points (a) T3, (b) Fpz, and (c) Cz for 45 subjects. The digits and characters in each matrix represent the identification number of subjects and brain regions, respectively. The color of the matrices in the upper panel of each subfigure for SBM and GMs indicates L_M and probability, respectively. The lower panel of each subfigure shows the difference in MLCBR between SBM and GMs. Red and green blocks indicate the MLCBR of SBM and GMs, respectively. When the MLCBR was consistent between SBM and GMs, the block turns yellow due to the additive color of green and red

corresponding brain regions using SBM, that is, MTG_L: 0.693; STG_L: 0.274; PoCG_L: 0.018. GM (S,S) and GM (S,T) displayed two cortical regions corresponding to T3, that is, MTG_L: 0.844 and 0.822; STG_L: 0.156 and 0.178, for GM (S,S) and GM (S,T), respectively, but we found T3 mapped to MTG_L for any subject by GM (T,T). For Fpz and Cz, the number of corresponding brain regions obtained by SBM was greater than that obtained by GMs. At Fpz, the probabilities of a few brain regions were much greater than those of others when GMs were used. In contrast, the probabilities were relatively even across the corresponding brain regions when SBM was used (see Table 2).

TABLE 2 The group-wise probabilities of the scalp-cortex correlation

		SBM (circumferential orientation)				
Fiducial point	AAL region	Mean	*SD*	GM (S,S)	GM (S,T)	GM (T,T)
T3	MTG-L	**.693**	.208	**.844**	**.822**	**1.000**
	STG-L	.274	.181	.156	.178	.000
	PoCG-L	.018	.028	.000	.000	.000
Fpz	ORBmed-R	**.291**	.109	**.578**	**.489**	**.478**
	ORBmed-L	.203	.073	.289	.156	.357
	SFGmed-R	.122	.078	.067	.244	.122
	SFGmed-L	.102	.068	.044	.111	.026
	ORBsup-L	.102	.065	.000	.000	.000
	ORBsup-R	.098	.067	.000	.000	.017
	SFGdor-L	.025	.022	.000	.000	.000
	SFGdor-R	.024	.023	.000	.000	.000
	REC-R	.011	.017	.000	.000	.000
	REC-L	.000	.000	.022	.000	.000
Cz	SMA-R	**.240**	.121	**.222**	.200	**.367**
	PCL-R	.168	.121	.178	**.267**	.114
	SFGdor-L	.155	.121	.200	.044	.000
	PCL-L	.153	.102	.178	.244	.359
	SMA-L	.115	.082	.178	.200	.159
	PreCG-L	.060	.073	.022	.000	.000
	PreCG-R	.046	.059	.022	.022	.000
	SFGdor-R	.038	.046	.000	.022	.000
	PoCG-L	.000	.000	.000	.000	.000

Note: The maximum value obtained by each matching method at each fiducial point is shown in bold. The group-wise MLCBR is the AAL region corresponding to the maximum value of each matching method. Abbreviation: *SD*, standard deviation.

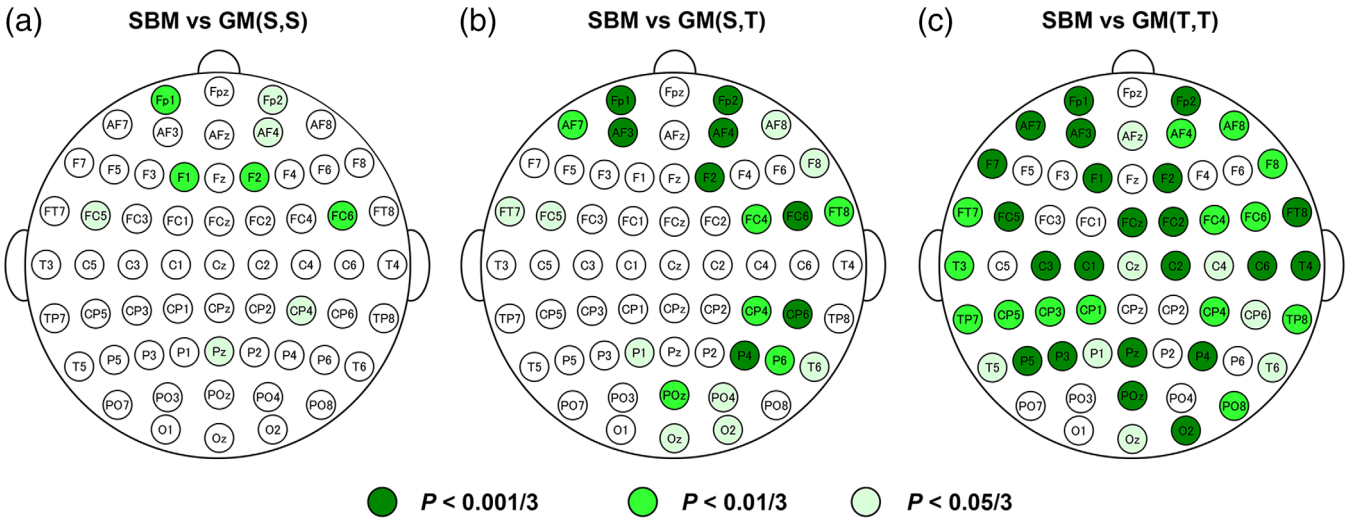

FIGURE 8 The differences for the group-wise probability between sensitivity-based matching (SBM) and each geometrical matching (GM) for all 10–10 fiducial points. (a) SBM versus GM (S,S); (b) SBM versus GM (S,T); (c) SBM versus GM (T,T). The color indicates the significant level of the chi-square test of independence after Dunnett's multiple comparison procedure. White circles indicate $p \geq .05/3$

The group-wise probabilities of all 10–10 fiducial points at the group level could be found in Table S2. The group-wise MLCBR at T3 and Fpz was kept consistent whichever method was adopted. In contrast, the group-wise MLCBR of GM (S,T) at Cz was different from that of the other three methods.

To assess the differences for the SCC quantitatively at all fiducial points at the group level, we performed a chi-square test of independence to examine whether group-wise probability for a given fiducial point derived from SBM and each GM was independent. When comparing results obtained from SBM and GM (S,S), we found that the group-wise probability was significantly different for 9 of 61 fiducial points (Figure 8a, fiducial points filled with color), which were mainly located in the anterior regions of the head. Furthermore, we found that 23 fiducial points mainly in anterior and posterior regions displayed a significant difference between SBM and GM (S,T) (Figure 8b). Intriguingly, the comparison between SBM and GM (T,T) showed that the group-wise probability was significantly different for 44 of 61 fiducial points, covering almost the whole head (Figure 8c).

For all fiducial points, the consistency of the MLCBR between SBM and each GM was assessed by the concordance rate Q. As shown in Figure 9, the MLCBR was moderately or highly consistent between SBM and GMs for most fiducial points. Importantly, the greater the methodological disassociation between SBM and GMs, the lower concordance rate Q was at almost all fiducial points. The mean and standard deviation of the concordance rate Q for all 10–10 fiducial points were 85.9 ± 11.2%, 74.0 ± 18.0%, and 65.5 ± 22.4% for SBM versus GM (S,S), SBM versus GM (S,T), and SBM versus GM (T,T), respectively. The concordance rate Q showed characteristic spatial distribution. The values were relatively low at frontal, central, and posterior fiducial points, particularly in SBM versus GM (S,T) and SBM versus GM (T,T).

4 | DISCUSSION

To date, most efforts to specify the cortical region under the scalp position in fNIRS studies have been based on a simple assumption that the signal originates from the brain region just below the midpoint of the emission and detection probes. Additionally, few studies investigated the role of inter-subject variations in the anatomical structure of the head and brain when in the SCC analysis. In the current study, we established a precise correlation between the sensitivity of probe pairs at 10–10 system positions on the head surface and brain regions contributing to the detected hemodynamic changes by analyzing light propagation in 45 subject-specific head models. We found that fNIRS sensitivity obtained by SBM was broadly distributed in several adjacent brain regions for all fiducial points on the scalp surface, and the sensitivity-based correlation was independent of probe-pair orientations but varied across subjects for the same fiducial point. The comparisons between sensitivity-based correlation and geometrical correlations demonstrated that matching methods had a significant influence on the SCC and that the level of influence was different for each fiducial point. In particular, the methodological dissociations between SBM and each GM determined the level of difference of the SCC. All of these findings demonstrated that it is necessary to consider both light scattering in head tissues and individual anatomical differences when estimating the brain region in which fNIRS signals originate.

4.1 | Methodological verification

We calculated the sensitivity-based correlation based on the diffusion equation. The diffusion equation has the advantage of reduced

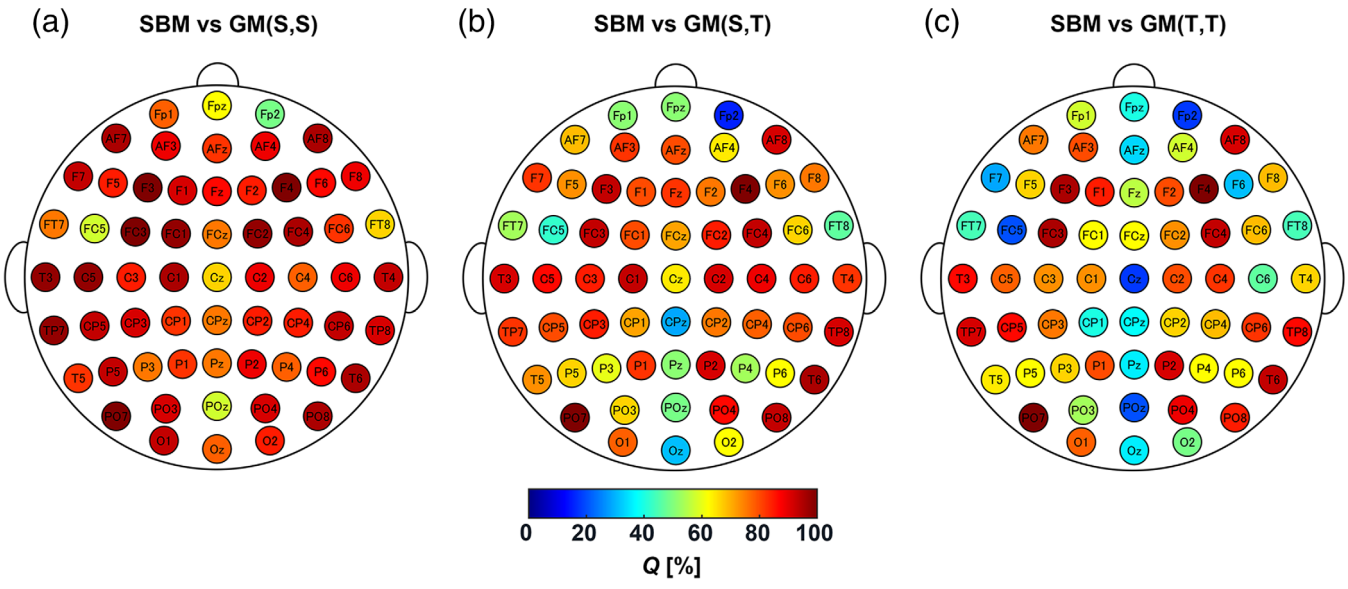

FIGURE 9 The consistency for the MLCBR at all fiducial points between sensitivity-based matching (SBM) and each geometrical matching (GM). (a) SBM versus GM (S,S), (b) SBM versus GM (S,T), and (c) SBM versus GM (T,T). A higher concordance rate Q correlated to a larger the number of subjects in which the most likely corresponding brain region (MLCBR) was the same between SBM and each GM

computation time compared to the Monte Carlo method, which is an essential component of the current study containing many subjects and a large number of scalp positions. Although the diffusion approximation cannot rigorously model light propagation in low-level scattering regions such as the CSF, previous studies have shown that there is no significant difference between the deterministic approach with the diffusion equation and the stochastic Monte Carlo method when the transport scattering coefficient of the CSF layer is more than .3 mm^{-1} (Koyama et al., 2005; Oki et al., 2009). We used a transport scattering coefficient of CSF at .3 mm^{-1} for light propagation calculations according to the precise optical modeling of the subarachnoid space (Okada & Delpy, 2003a). Therefore, the PMDF and the L_M obtained by our calculations must be similar to those obtained by the Monte Carlo method.

The accuracy of the L_M is also affected by the parcellation accuracy of the gray matter in the brain regions. Since the AAL atlas uses the sulcus as a boundary to parcellate brain regions, the accuracy of the parcellation on the individual brain can be easily evaluated by visual assessment. It should be noted that the AAL atlas is based on the Colin27 average brain, created by scanning a single subject 27 times (Holmes et al., 1998). Previous studies have demonstrated that the single-subject AAL atlas does not adequately represent the partition pattern of the human brain because it cannot capture the neuroanatomical variability across individuals (Devlin & Poldrack, 2007) and does not match the cytoarchitectonic borders well in most cases (Amunts, Schleicher, & Zilles, 2007). Despite these limitations, we still utilized the AAL atlas to calculate the SCC for the purpose of direct comparison between SBM and GMs, for which the AAL atlas is usually employed. Given that the AAL atlas is represented on standard brain structures, we tried to parcellate individual gray matter by transforming a standard brain structure into an individual brain structure using the DARTEL method. However, upon applying this method by itself, a brain region located in a certain sulcus in the standard brain was incorrectly transferred into several gyri in the individual brain (data not shown). To improve parcellation, the RBFT was applied after using the DARTEL method to accurately align the 17 major cerebral sulci on the standard and individual brain structures. The application of DARTEL followed by RBFT provided accurate parcellation of the individual gray matter into the AAL brain regions. Therefore, the L_M is accurate for the current brain region parcellation. Importantly, SBM is not restricted to the AAL atlas; other atlases such as the Brodmann atlas (Brodmann, 2006) or the HCP-MMP1.0 atlas (Glasser et al., 2016) could also be applied when calculating the SCC using the SBM method. Thus, future work could consider establishing a sensitivity-based correlation using other atlases to help understand human brain function.

4.2 | Impact of light propagation in tissue on SCC

The SCC obtained from SBM always displayed multiple corresponding brain regions for a fiducial point. Particularly, a certain single brain region dominated the L_M for some fiducial points such as T3 and T4, while several brain regions possessed the equivalent L_M at other fiducial points above the longitudinal fissure such as Fpz and Cz. Thus, the source of the fNIRS signal could be estimated exactly based on the scalp position when the probe pair is attached around the former fiducial points, whereas such estimation is difficult when the probe pair is attached around the latter fiducial points. For the interpretation of fNIRS data measured around at the latter points, meticulous attention should be paid to the brain region in which activity occurs.

Interestingly, the probe-pair orientation had no significant influence on the distribution of L_M over 10–10 positions, which was consistent with findings from photon propagation in the Colin27 brain template (Strangman, Zhang, & Li, 2014). Regardless of the probe-pair orientation, the PMDF value in the gray matter showed the local maximum at just below the midpoint of the emission and detection probes and decreased with increasing distance from the maximum point. In addition, the contour lines of the PMDF on the gray matter surface resembled concentric circles centered at the maximum point. These spatial features of the PMDF explain the fact that the SCC is independent of the orientation of the probe pairs. It is a welcome relief for fNIRS users that the orientation of the probe pair has little effect on the sensitivity-based correlation. On the other hand, the spatial features of the PMDF depend on the distance between the emission and detection probes. Thus, it is uncertain whether such spatial features of the PMDF would change when the emission-detection spacings were not 30 mm. Previous studies have suggested that the optimal emission-detection spacing should be narrowed down to 30–35 mm (Chuang, Chen, Hsieh, Liu, & Sun, 2013; T. Li, Gong, & Luo, 2011; Strangman et al., 2013), while different adult brains had their own optimal emission-detection spacing (Chuang et al., 2013). How the interaction between individual brain structure and emission-detection spacing affects SCC might be an interesting future research question.

In addition to the emission-detection spacing, the SSP of fNIRS is sensitive to individual anatomical differences associated with variations in head size, depth of the brain from the scalp, among other factors. Such individual anatomical difference is illustrated by evidence that each individual subject exhibits unique scalp and skull thickness, CSF distributions and cortical folding patterns (Hasan et al., 2007; H. Li, Ruan, Xie, Wang, & Liu, 2007). Moreover, a recent study provided direct evidence supporting our findings, because the partial optical pathlength in the brain decreases with an increase in the scalp-brain distance varying with individuals and across brain regions (Nakamura et al., 2016).

In particular, nonbrain superficial head tissues, such as scalp, skull or CSF, could have a considerable influence on the SSP. Evidence from light propagation analysis in the adult head revealed that a low-scattering CSF layer could significantly broaden the SSP and confine the SSP of the sampling areas to the shallow regions of the gray matter (Firbank et al., 1998; Okada et al., 1997). In addition, the SSP is significantly affected by the thickness of the CSF layer (Okada & Delpy, 2003b). In older adults, changes in the thickness of the CSF layer due to brain atrophy could result in a decrease in sensitivity as the scalp-brain distance increases. Similarly, Beauchamp et al. documented changes in the scalp-brain distance with age in 71 children

aged 0–12 years old (Beauchamp et al., 2011). These age-related anatomical changes had an effect on the optical path in tissue and the fraction of the signal coming from the actual brain compared to the superficial layers (Whiteman, Santosa, Chen, Perlman, & Huppert, 2018). Since the age range of subjects in this study was 21–58 years, the sensitivity-based correlation in the other age groups should also be considered.

In recent years, the short channel regression technique has been applied in fNIRS studies to isolate the cortical functional response by regressing the noise from superficial tissues, such as the scalp and skull, from the standard fNIRS signal (Brigadoi & Cooper, 2015; Saager & Berger, 2005). Notably, short channel regression has been demonstrated as an effective method for the removal of systemic physiological artifacts in fNIRS data analysis (Santosa, Zhai, Fishburn, Sparto, & Huppert, 2020; Wyser et al., 2020; Yücel et al., 2015). The short channel regression assumes that the signal received at the short separation detector is mostly representative of the superficial layers, while the signal received at the long separation detector is sensitive to both the brain and superficial layers. Thus, regression of the short separation signal from the long separation signal effectively filters out the superficial component, whereas it has no influence on the signal from the brain. In addition, the SBM-derived SCC was only from the sensitivity in the gray matter. These facts indicate that short channel regression does not affect the SCC obtained by SBM. Sensitivity-based correlation is useful for fNIRS studies, regardless of the use of short distance regression.

4.3 | Comparison of SCCs between matching methods

In the present study, we compared the SCC of three GMs with that of SBM. Remarkably, we found that the smaller the methodological dissociation between SBM and GMs, the smaller the number of fiducial points that displayed significantly different group-wise probability of the SCC between SBM and GM, and the larger the number of subjects in which the MLCBR was consistent between SBM and GM. As per the description in Section 2.3.2, GM (S,S) is completely the same as SBM except for ignoring light scattering. There were the smallest differences between GM(S,S) and SBM in terms of the group-wise probability and the MLCBR. We found the group-wise probability showed statistically significant differences between SBM and GM (S,S) at 14.8% of all fiducial points. At such fiducial points, the influence of light propagation cannot be ignored to obtain the SCC accurately. On the other hand, the MLCBR of SBM and GM (S,S) showed relatively high consistency across almost all fiducial points and individual subjects. If we accept the assumption that brain activation is confined to a single brain region, GM (S,S) could provide a reasonable signal source for fNIRS.

GM (S,T) had a greater deviation from SBM than GM (S,S) with regards to the SCC. GM (S,T) is methodologically different from GM (S,S) at the point that assigning brain regions in the template space after the spatial normalization, which indicates that the accuracy of spatial normalization strongly affects the SCC. Similar spatial normalization was included in the process to construct the transcranial brain atlas (Xiao et al., 2018). A more sophisticated transcranial brain atlas could be constructed by either replacing the spatial normalization with other more accurate techniques such as DARTEL followed by RBFT, or using the SCC from GM (S,S).

GM (T,T) displayed the largest discrepancy with SBM. There were statistically significant differences in the group-wise probabilities between SBM and GM (T,T) at 72.1% of all fiducial points. Characteristically, GM (T,T) showed fewer individual differences on the SCC than the other matching methods (Figure 7). In other words, GM (T,T) eliminates the individual differences of the SCC that actually exist. In GM (T,T), a point on the scalp of the individual subject was transferred to the template space by the affine transformation that aligns the fiducial points in the individual space with those of the template space. Then, the transferred point was projected onto the cortical surface in the template space. Noticeably, the head structures of the same 17 subjects are always used in GM (T,T), which indicates the positional relationship between the scalp and cortical surface is stationary on the SCC analysis by GM (T,T) for any subjects.

4.4 | Consideration of appropriate SCC for fNIRS

The SCC aims to identify cortical activation regions caused by changes in absorbance measured at the probe pairs attached to the scalp. Essentially, the SCC should be analyzed on the subject-specific anatomical structure because it is influenced by individual differences. However, the anatomical structures of individual subjects are not available in most fNIRS experiments. Techniques such as probabilistic registration and the transcranial brain atlas have been developed to estimate the activation region in such cases. Probabilistic registration is GM (T,T) itself, and a method equivalent to GM (S,T) was used to construct the transcranial brain atlas. We revealed the SCC of these two methods was significantly different from that of SBM at a considerable number of fiducial points. Therefore, at those fiducial points, the reliability of the SCC obtained by GM (T,T) or GM (S,T) should be evaluated with great care.

The group-wise probability of the SCC obtained by SBM and GM (S,S) could be a promising alternative to the SCC on the individual subject. The group-wise probability of SBM consists of individual SCCs considering the effects of light propagation in the head of 45 subjects. The full list of brain regions where the group-wise probability was greater than zero encompassed the brain regions that are potential sources of the fNIRS signal at each fiducial point. Thus, the possibility of ignoring the activation region must be extremely small by referring to the group-wise probability of SBM. In addition to SBM, GM (S,S) is also useful for estimating a brain region that is most likely to be activated for a fiducial point because the MLCBR obtained by SBM and GM (S,S) was almost identical.

As we discussed previously, the group-wise probability of the SCC obtained by SBM (Table S2) could be used as a lookup table to guide fNIRS users to design their probe geometry for targeting

specific brain regions and thus help to more precisely explain fNIRS data obtained according to the 10–10 system. Although the group-wise probability of the SCC from SBM was greater than 0 in all brain regions adjacent to the skull, except for subcortical regions of the brain, the spatial density of the 10–10 fiducial points for analyzing the sensitivity-based correlation would be relatively sparse because a few brain regions had only a small chance of being corresponded. The sensitivity-based correlation calculated over all fiducial points of a denser placement system (Oostenveld & Praamstra, 2001) can keep all brain regions with a high probability of being corresponded. The group-wise probability obtained by SBM with a denser placement system can provide the corresponding brain regions of fNIRS probes placed anywhere on the scalp.

The currently proposed SBM method can be implemented into fNIRS and diffuse optical tomography (DOT). In some fNIRS measurements, the 3D coordinates of optodes on the scalp can be determined by instruments such as a 3D digitizer. By virtual positioning of the optodes on the heads of 45 subjects, SBM could be utilized to calculate the SCC based on light propagation from 45 subject-specific head models to approximately reach the required accuracy using the subject's own MRI. That is, it is possible to obtain a fairly accurate SCC even without the subject's head structure. Notably, the SBM method is useful not only for fNIRS measurements, but also for DOT, which utilizes a large number of densely placed emission-detection probe arrangements and allows the reconstruction of 3D images of brain activation by solving the inverse problem (Culver, Siegel, Stott, & Boas, 2003). Specifically, SBM will help correlate the reconstruction image of brain function by DOT and the underlying brain regions for a given probe arrangement. In addition, SBM could also contribute to the probe arrangement design for targeting specific brain regions in DOT, as well as to obtain the underlying brain regions for the long measurement channels.

5 | CONCLUSION

In this article, we provided compelling evidence demonstrating that light scattering and individual anatomical differences in the adult head affect the SCC in fNIRS, while the orientation of the probe pair has little effect. Importantly, the proposed SBM method could be used to obtain the precise SCC by considering both the light scattering in head tissues and individual anatomical differences, compared to the conventional GM methods, which may overlook brain regions that should have been essential candidates for the fNIRS signal source. For practical application, we recommend using group-wise probability, consisting of individual SCCs over 10–10 system positions obtained by the SBM method, to design probe arrangements to targeted brain regions of interest and explain fNIRS measurement data, since this index considers the effects of light propagation in the head of 45 subjects. Once the coordinates of optodes on the scalp are available, fNIRS users will be able to adopt the SBM method to estimate the underlying brain regions for any probe pair without the subject's own MRI.

ACKNOWLEDGMENT

The study was funded by the operating budgets of the authors' institutions.

CONFLICT OF INTEREST

All authors declare no competing financial interests.

AUTHOR CONTRIBUTIONS

Lin Cai: Conceptualization, Formal analysis, Writing - original draft, review & editing. **Tomonori Nitta:** Conceptualization, Formal analysis. **Sho Yokota:** Formal analysis. **Takayuki Obata:** Investigation, Resources. **Eiji Okada:** Conceptualization, Supervision, Writing - review & editing, Funding acquisition. **Hiroshi Kawaguchi:** Conceptualization, Investigation, Resources, Supervision, Writing - review & editing, Funding acquisition.

DATA AVAILABILITY STATEMENT

The data that support the findings of this study are available from the corresponding author upon reasonable request.

ORCID

Lin Cai https://orcid.org/0000-0002-5948-6872

Hiroshi Kawaguchi https://orcid.org/0000-0002-1496-2812

REFERENCES

Amunts, K., Schleicher, A., & Zilles, K. (2007). Cytoarchitecture of the cerebral cortex—More than localization. *NeuroImage*, *37*(4), 1061–1065.

Anderson, C. A., Wiggins, I. M., Kitterick, P. T., & Hartley, D. E. H. (2017). Adaptive benefit of cross-modal plasticity following cochlear implantation in deaf adults. *Proceedings of the National Academy of Sciences of the United States of America*, *114*(38), 10256–10261. https://doi.org/10.1073/pnas.1704785114

Arridge, S. R. (1995). Photon-measurement density functions. Part I: Analytical forms. *Applied Optics*, *34*(31), 7395–7409. https://doi.org/10.1364/AO.34.007395

Arridge, S. R., & Schweiger, M. (1995). Photon-measurement density functions. Part 2: Finite-element-method calculations. *Applied Optics*, *34*(34), 8026–8037. https://doi.org/10.1364/AO.34.008026

Ashburner, J. (2007). A fast diffeomorphic image registration algorithm. *NeuroImage*, *38*(1), 95–113. https://doi.org/10.1016/j.neuroimage.2007.07.007

Auzias, G., Colliot, O., Glaunes, J. A., Perrot, M., Mangin, J. F., Trouve, A., & Baillet, S. (2011). Diffeomorphic brain registration under exhaustive sulcal constraints. *IEEE Transactions on Medical Imaging*, *30*(6), 1214–1227. https://doi.org/10.1109/TMI.2011.2108665

Beauchamp, M. S., Beurlot, M. R., Fava, E., Nath, A. R., Parikh, N. A., Saad, Z. S., … Oghalai, J. S. (2011). The developmental trajectory of brain-scalp distance from birth through childhood: Implications for functional neuroimaging. *Plos One*, *6*(9), ARTN e24981. https://doi.org/10.1371/journal.pone.0024981

Bevilacqua, F., Piguet, D., Marquet, P., Gross, J. D., Tromberg, B. J., & Depeursinge, C. (1999). In vivo local determination of tissue optical properties: Applications to human brain. *Applied Optics*, *38*(22), 4939–4950. https://doi.org/10.1364/Ao.38.004939

Blume, W. T., Buza, R. C., & Okazaki, H. (1974). Anatomic correlates of the ten-twenty electrode placement system in infants. *Electroencephalography and Clinical Neurophysiology*, *36*(3), 303–307. https://doi.org/10.1016/0013-4694(74)90172-2

Boas, D. A., Elwell, C. E., Ferrari, M., & Taga, G. (2014). Twenty years of functional near-infrared spectroscopy: Introduction for the special issue. *NeuroImage*, *85*, 1–5. https://doi.org/10.1016/j.neuroimage.2013.11.033

Brigadoi, S., & Cooper, R. J. (2015). How short is short? Optimum source-detector distance for short-separation channels in functional near-infrared spectroscopy. *Neurophotonics*, *2*(2), 025005. https://doi.org/10.1117/1.NPh.2.2.025005

Brodmann, K., & Garey, L. J. (2006). *Brodmann's Localisation in the Cerebral Cortex*, New York, NY: Springer Science.

Cai, L., Dong, Q., & Niu, H. J. (2018). The development of functional network organization in early childhood and early adolescence: A resting-state fNIRS study. *Developmental Cognitive Neuroscience*, *30*, 223–235. https://doi.org/10.1016/j.dcn.2018.03.003

Cai, L., Dong, Q., Wang, M. J., & Niu, H. J. (2019). Functional near-infrared spectroscopy evidence for the development of topological asymmetry between hemispheric brain networks from childhood to adulthood. *Neurophotonics*, *6*(2), ARTN 025005. https://doi.org/10.1117/1.NPh.6.2.025005

Chuang, C. C., Chen, C. M., Hsieh, Y. S., Liu, T. C., & Sun, C. W. (2013). Brain structure and spatial sensitivity profile assessing by near-infrared spectroscopy modeling based on 3D MRI data. *Journal of Biophotonics*, *6*(3), 267–274. https://doi.org/10.1002/jbio.201200025

Culver, J. P., Siegel, A. M., Stott, J. J., & Boas, D. A. (2003). Volumetric diffuse optical tomography of brain activity. *Optics Letters*, *28*(21), 2061–2063.

Custo, A., Wells, W. M., Barnett, A. H., Hillman, E. M. C., & Boas, D. A. (2006). Effective scattering coefficient of the cerebral spinal fluid in adult head models for diffuse optical imaging. *Applied Optics*, *45*(19), 4747–4755. https://doi.org/10.1364/Ao.45.004747

Cutini, S., Scatturin, P., & Zorzi, M. (2011). A new method based on ICBM152 head surface for probe placement in multichannel fNIRS. *NeuroImage*, *54*(2), 919–927.

Dehghani, H., Eames, M. E., Yalavarthy, P. K., Davis, S. C., Srinivasan, S., Carpenter, C. M., … Paulsen, K. D. (2009). Near infrared optical tomography using NIRFAST: Algorithm for numerical model and image reconstruction. *Communications in Numerical Methods in Engineering*, *25*(6), 711–732. https://doi.org/10.1002/cnm.1162

Devlin, J. T., & Poldrack, R. A. (2007). In praise of tedious anatomy. *NeuroImage*, *37*(4), 1033–1041.

Dunnett, C. W. (1955). A multiple comparison procedure for comparing several treatments with a control. *Journal of the American Statistical Association*, *50*(272), 1096–1121.

Fang, Q. Q., & Boas, D. A. (2009). *Tetrahedral Mesh Generation from Volumetric Binary and Gray-Scale Images*. 2009 IEEE International Symposium on Biomedical Imaging: From Nano to Macro, Vols 1 and 2, 1142-1145.doi: https://doi.org/10.1109/Isbi.2009.5193259

Firbank, M. (1994). *The design, calibration and usage of a solid scattering and absorbing phantom for near infra red spectroscopy*. London, England: University of London.

Firbank, M., Okada, E., & Delpy, D. T. (1998). A theoretical study of the signal contribution of regions of the adult head to near-infrared spectroscopy studies of visual evoked responses. *NeuroImage*, *8*(1), 69–78. https://doi.org/10.1006/nimg.1998.0348

Fukui, Y., Ajichi, Y., & Okada, E. (2003). Monte Carlo prediction of near-infrared light propagation in realistic adult and neonatal head models. *Applied Optics*, *42*(16), 2881–2887. https://doi.org/10.1364/Ao.42.002881

Gebhart, S. C., Lin, W. C., & Mahadevan-Jansen, A. (2006). In vitro determination of normal and neoplastic human brain tissue optical properties using inverse adding-doubling. *Physics in Medicine and Biology*, *51*(8), 2011–2027. https://doi.org/10.1088/0031-9155/51/8/004

Glasser, M. F., Coalson, T. S., Robinson, E. C., Hacker, C. D., Harwell, J., Yacoub, E., … Jenkinson, M. (2016). A multi-modal parcellation of human cerebral cortex. *Nature*, *536*(7615), 171–178.

Hale, G. M., & Querry, M. R. (1973). Optical constants of water in the 200-nm to 200-microm wavelength region. *Applied Optics*, *12*(3), 555–563. https://doi.org/10.1364/AO.12.000555

Hasan, K. M., Sankar, A., Halphen, C., Kramer, L. A., Brandt, M. E., Juranek, J., … Ewing-Cobbs, L. (2007). Development and organization of the human brain tissue compartments across the lifespan using diffusion tensor imaging. *Neuroreport*, *18*(16), 1735–1739.

Holmes, C. J., Hoge, R., Collins, L., Woods, R., Toga, A. W., & Evans, A. C. (1998). Enhancement of MR images using registration for signal averaging. *Journal of Computer Assisted Tomography*, *22*(2), 324–333.

Homan, R. W., Herman, J., & Purdy, P. (1987). Cerebral location of international 10-20 system electrode placement. *Electroencephalography and Clinical Neurophysiology*, *66*(4), 376–382. https://doi.org/10.1016/0013-4694(87)90206-9

Hoshi, Y., Shimada, M., Sato, C., & Iguchi, Y. (2005). Reevaluation of near-infrared light propagation in the adult human head: Implications for functional near-infrared spectroscopy. *Journal of Biomedical Optics*, *10*(6), 064032. https://doi.org/10.1117/1.2142325

Huang, Y., Parra, L. C., & Haufe, S. (2016). The New York Head—A precise standardized volume conductor model for EEG source localization and tES targeting. *NeuroImage*, *140*, 150–162.

Jermyn, M., Ghadyani, H., Mastanduno, M. A., Turner, W., Davis, S. C., Dehghani, H., & Pogue, B. W. (2013). Fast segmentation and high-quality three-dimensional volume mesh creation from medical images for diffuse optical tomography. *Journal of Biomedical Optics*, *18*(8), 086007. https://doi.org/10.1117/1.Jbo.18.8.086007

Jiang, J., Chen, C., Dai, B., Shi, G., Ding, G., Liu, L., & Lu, C. (2015). Leader emergence through interpersonal neural synchronization. *Proceedings of the National Academy of Sciences of the United States of America*, *112*(14), 4274–4279. https://doi.org/10.1073/pnas.1422930112

Jurcak, V., Tsuzuki, D., & Dan, I. (2007). 10/20, 10/10, and 10/5 systems revisited: Their validity as relative head-surface-based positioning systems. *NeuroImage*, *34*(4), 1600–1611. https://doi.org/10.1016/j.neuroimage.2006.09.024

Kawaguchi, H., Hayashi, T., Kato, T., & Okada, E. (2004). Theoretical evaluation of accuracy in position and size of brain activity obtained by near-infrared topography. *Physics in Medicine & Biology*, *49*(12), 2753–2765.

Keller, P. J., Hunter, W., Jr., & Schmalbrock, P. (1987). Multisection fat-water imaging with chemical shift selective presaturation. *Radiology*, *164*(2), 539–541.

Koessler, L., Maillard, L., Benhadid, A., Vignal, J. P., Felblinger, J., Vespignani, H., & Braun, M. (2009). Automated cortical projection of EEG sensors: Anatomical correlation via the international 10-10 system. *NeuroImage*, *46*(1), 64–72. https://doi.org/10.1016/j.neuroimage.2009.02.006

Kovelman, I., Shalinsky, M. H., White, K. S., Schmitt, S. N., Berens, M. S., Paymer, N., & Petitto, L. A. (2009). Dual language use in sign-speech bimodal bilinguals: fNIRS brain-imaging evidence. *Brain and Language*, *109*(2–3), 112–123. https://doi.org/10.1016/j.bandl.2008.09.008

Koyama, T., Iwasaki, A., Ogoshi, Y., & Okada, E. (2005). Practical and adequate approach to modeling light propagation in an adult head with low-scattering regions by use of diffusion theory. *Applied Optics*, *44*(11), 2094–2103. https://doi.org/10.1364/Ao.44.002094

Kurihara, K., Kawaguchi, H., Obata, T., Ito, H., & Okada, E. (2015). Magnetic resonance imaging appropriate for construction of subject-specific head models for diffuse optical tomography. *Biomedical Optics Express*, *6*(9), 3197–3209. https://doi.org/10.1364/Boe.6.003197

Li, H., Ruan, J., Xie, Z., Wang, H., & Liu, W. (2007). Investigation of the critical geometric characteristics of living human skulls utilising medical image analysis techniques. *International Journal of Vehicle Safety*, *2*(4), 345–367.

Li, T., Gong, H., & Luo, Q. (2011). Visualization of light propagation in visible Chinese human head for functional near-infrared spectroscopy. *Journal of Biomedical Optics*, *16*(4), 045001 Retrieved from https://

www.spiedigitallibrary.org/journals/Journal-of-Biomedical-Optics/volume-16/issue-4/045001/Visualization-of-light-propagation-in-visible-Chinese-human-head-for/10.1117/1.3567085.pdf

Lloyd-Fox, S., Blasi, A., & Elwell, C. E. (2010). Illuminating the developing brain: The past, present and future of functional near infrared spectroscopy. *Neuroscience and Biobehavioral Reviews*, *34*(3), 269–284. https://doi.org/10.1016/j.neubiorev.2009.07.008

Machado, A., Cai, Z., Pellegrino, G., Marcotte, O., Vincent, T., Lina, J. M., … Grova, C. (2018). Optimal positioning of optodes on the scalp for personalized functional near-infrared spectroscopy investigations. *Journal of Neuroscience Methods*, *309*, 91–108. https://doi.org/10.1016/j.jneumeth.2018.08.006

Minagawa, Y., Xu, M. D., & Morimoto, S. (2018). Toward interactive social neuroscience: Neuroimaging real-world interactions in various populations. *Japanese Psychological Research*, *60*(4), 196–224. https://doi.org/10.1111/jpr.12207

Minagawa-Kawai, Y., Mori, K., Naoi, N., & Kojima, S. (2007). Neural attunement processes in infants during the acquisition of a language-specific phonemic contrast. *Journal of Neuroscience*, *27*(2), 315–321. https://doi.org/10.1523/Jneurosci.1984-06.2007

Morais, G. A. Z., Balardin, J. B., & Sato, J. R. (2018). fNIRS optodes' location decider (fOLD): A toolbox for probe arrangement guided by brain regions-of-interest. *Scientific Reports*, *8*, ARTN 3341. https://doi.org/10.1038/s41598-018-21716-z

Moriguchi, Y., & Hiraki, K. (2009). Neural origin of cognitive shifting in young children. *Proceedings of the National Academy of Sciences of the United States of America*, *106*(14), 6017–6021. https://doi.org/10.1073/pnas.0809747106

Nakamura, K., Kurihara, K., Kawaguchi, H., Obata, T., Ito, H., & Okada, E. (2016). Estimation of partial optical path length in the brain in subject-specific head models for near-infrared spectroscopy. *Optical Review*, *23*(2), 316–322. https://doi.org/10.1007/s10043-016-0179-9

Okada, E., & Delpy, D. T. (2003a). Near-infrared light propagation in an adult head model. I. Modeling of low-level scattering in the cerebrospinal fluid layer. *Applied Optics*, *42*(16), 2906–2914. https://doi.org/10.1364/Ao.42.002906

Okada, E., & Delpy, D. T. (2003b). Near-infrared light propagation in an adult head model. II. Effect of superficial tissue thickness on the sensitivity of the near-infrared spectroscopy signal. *Applied Optics*, *42*(16), 2915–2922. https://doi.org/10.1364/Ao.42.002915

Okada, E., Firbank, M., Schweiger, M., Arridge, S. R., Cope, M., & Delpy, D. T. (1997). Theoretical and experimental investigation of near-infrared light propagation in a model of the adult head. *Applied Optics*, *36*(1), 21–31. https://doi.org/10.1364/ao.36.000021

Okamoto, M., Dan, H., Sakamoto, K., Takeo, K., Shimizu, K., Kohno, S., … Dan, I. (2004). Three-dimensional probabilistic anatomical cranio-cerebral correlation via the international 10-20 system oriented for transcranial functional brain mapping. *NeuroImage*, *21*(1), 99–111. https://doi.org/10.1016/j.neuroimage.2003.08.026

Okamoto, M., & Dan, I. (2005). Automated cortical projection transcranial functional brain of head-surface locations for mapping. *NeuroImage*, *26*(1), 18–28. https://doi.org/10.1016/j.neuroimage.2005.01.018

Oki, Y., Kawaguchi, H., & Okada, E. (2009). Validation of practical diffusion approximation for virtual near infrared spectroscopy using a digital head phantom. *Optical Review*, *16*(2), 153–159.

Okamoto, M., & Dan, I. (2005). Automated cortical projection of head-surface locations for transcranial functional brain mapping. *Neuroimage*, *26*(1), 18–28.

Oostenveld, R., & Praamstra, P. (2001). The five percent electrode system for high-resolution EEG and ERP measurements. *Clinical Neurophysiology*, *112*(4), 713–719. https://doi.org/10.1016/S1388-2457(00)00527-7

Pighin, F., Hecker, J., Lischinski, D., Szeliski, R., & Salesin, D. H. (2006). *Synthesizing Realistic Facial Expressions from Photographs*. Paper presented at the ACM SIGGRAPH 2006 Courses.

Quaresima, V., Bisconti, S., & Ferrari, M. (2012). A brief review on the use of functional near-infrared spectroscopy (fNIRS) for language imaging studies in human newborns and adults. *Brain and Language*, *121*(2), 79–89. https://doi.org/10.1016/j.bandl.2011.03.009

Quaresima, V., & Ferrari, M. (2019). A mini-review on functional near-infrared spectroscopy (fNIRS): Where do we stand, and where should we go? *Photonics*, *6*(3), ARTN 87. https://doi.org/10.3390/photonics6030087

Rolls, E. T., Joliot, M., & Tzourio-Mazoyer, N. (2015). Implementation of a new parcellation of the orbitofrontal cortex in the automated anatomical labeling atlas. *NeuroImage*, *122*, 1–5. https://doi.org/10.1016/j.neuroimage.2015.07.075

Saager, R. B., & Berger, A. J. (2005). Direct characterization and removal of interfering absorption trends in two-layer turbid media. *JOSA A*, *22*(9), 1874–1882.

Sakakibara, Y., Kurihara, K., & Okada, E. (2016). Evaluation of improvement of diffuse optical imaging of brain function by high-density probe arrangements and imaging algorithms. *Optical Review*, *23*(2), 346–353.

Saliba, J., Bortfeld, H., Levitin, D. J., & Oghalai, J. S. (2016). Functional near-infrared spectroscopy for neuroimaging in cochlear implant recipients. *Hearing Research*, *338*, 64–75. https://doi.org/10.1016/j.heares.2016.02.005

Santosa, H., Zhai, X., Fishburn, F., Sparto, P. J., & Huppert, T. J. (2020). Quantitative comparison of correction techniques for removing systemic physiological signal in functional near-infrared spectroscopy studies. *Neurophotonics*, *7*(3), 035009.

Schmitz, B., Hagen, T., & Reith, W. (2003). Three-dimensional true FISP for high-resolution imaging of the whole brain. *European Radiology*, *13*(7), 1577–1582.

Scholkmann, F., Kleiser, S., Metz, A. J., Zimmermann, R., Pavia, J. M., Wolf, U., & Wolf, M. (2014). A review on continuous wave functional near-infrared spectroscopy and imaging instrumentation and methodology. *NeuroImage*, *85*, 6–27. https://doi.org/10.1016/j.neuroimage.2013.05.004

Singh, A. K., Okamoto, M., Dan, H., Jurcak, V., & Dan, I. (2005). Spatial registration of multichannel multi-subject fNIRS data to MNI space without MRI. *NeuroImage*, *27*(4), 842–851. https://doi.org/10.1016/j.neuroimage.2005.05.019

Strangman, G., Franceschini, M. A., & Boas, D. A. (2003). Factors affecting the accuracy of near-infrared spectroscopy concentration calculations for focal changes in oxygenation parameters. *NeuroImage*, *18*(4), 865–879. https://doi.org/10.1016/S1053-8119(03)00021-1

Strangman, G. E., Li, Z., & Zhang, Q. (2013). Depth sensitivity and source-detector separations for near infrared spectroscopy based on the Colin27 brain template. *PLoS One*, *8*(8), e66319. https://doi.org/10.1371/journal.pone.0066319

Strangman, G. E., Zhang, Q., & Li, Z. (2014). Scalp and skull influence on near infrared photon propagation in the Colin27 brain template. *NeuroImage*, *85*, 136–149. https://doi.org/10.1016/j.neuroimage.2013.04.090

Torricelli, A., Pifferi, A., Taroni, P., Giambattistelli, E., & Cubeddu, R. (2001). In vivo optical characterization of human tissues from 610 to 1010 nm by time-resolved reflectance spectroscopy. *Physics in Medicine and Biology*, *46*(8), 2227–2237. https://doi.org/10.1088/0031-9155/46/8/313

Tsuzuki, D., & Dan, I. (2014). Spatial registration for functional near-infrared spectroscopy: From channel position on the scalp to cortical location in individual and group analyses. *NeuroImage*, *85*, 92–103. https://doi.org/10.1016/j.neuroimage.2013.07.025

Tsuzuki, D., Jurcak, V., Singh, A. K., Okamoto, M., Watanabe, E., & Dan, I. (2007). Virtual spatial registration of stand-alone fNIRS data to MNI space. *NeuroImage*, *34*(4), 1506–1518. https://doi.org/10.1016/j.neuroimage.2006.10.043

Tzourio-Mazoyer, N., Landeau, B., Papathanassiou, D., Crivello, F., Etard, O., Delcroix, N., … Joliot, M. (2002). Automated anatomical

labeling of activations in SPM using a macroscopic anatomical parcellation of the MNI MRI single-subject brain. *NeuroImage*, *15*(1), 273–289. https://doi.org/10.1006/nimg.2001.0978

Vitorio, R., Stuart, S., Rochester, L., Alcock, L., & Pantall, A. (2017). fNIRS response during walking—Artefact or cortical activity? A systematic review. *Neuroscience and Biobehavioral Reviews*, *83*, 160–172. https://doi.org/10.1016/j.neubiorev.2017.10.002

Whiteman, A. C., Santosa, H., Chen, D. F., Perlman, S., & Huppert, T. (2018). Investigation of the sensitivity of functional near-infrared spectroscopy brain imaging to anatomical variations in 5- to 11-year-old children. *Neurophotonics*, *5*(1), ARTN 011009. https://doi.org/10.1117/1.NPh.5.1.011009

Wyser, D., Mattille, M., Wolf, M., Lambercy, O., Scholkmann, F., & Gassert, R. (2020). Short-channel regression in functional near-infrared spectroscopy is more effective when considering heterogeneous scalp hemodynamics. *Neurophotonics*, *7*(3), 035011.

Xiao, X., Yu, X. T., Zhang, Z., Zhao, Y., Jiang, Y. H., Li, Z., … Zhu, C. Z. (2018). Transcranial brain atlas. *Science Advances*, *4*(9), ARTN eaar6904. https://doi.org/10.1126/sciadv.aar6904

Yücel, M. A., Selb, J., Aasted, C. M., Petkov, M. P., Becerra, L., Borsook, D., & Boas, D. A. (2015). Short separation regression improves statistical significance and better localizes the hemodynamic response obtained by near-infrared spectroscopy for tasks with differing autonomic responses. *Neurophotonics*, *2*(3), 035005.

Zhang, Y. Y., Brady, M., & Smith, S. (2001). Segmentation of brain MR images through a hidden Markov random field model and the expectation-maximization algorithm. *IEEE Transactions on Medical Imaging*, *20*(1), 45–57. https://doi.org/10.1109/42.906424

SUPPORTING INFORMATION

Additional supporting information may be found online in the Supporting Information section at the end of this article.

How to cite this article: Cai L, Nitta T, Yokota S, Obata T, Okada E, Kawaguchi H. Targeting brain regions of interest in functional near-infrared spectroscopy—Scalp-cortex correlation using subject-specific light propagation models. *Hum Brain Mapp*. 2021;42:1969–1986. https://doi.org/10.1002/hbm.25367